Received 1 March 2023; revised 22 April 2023; accepted 14 May 2023. Date of publication 23 May 2023; date of current version 1 June 2023.

Digital Object Identifier 10.1109/OJAP.2023.3279090

3D Printed Hemispherically Radiating Antenna for Broadband Millimeter Wave Applications

LUKAS ENGEL (Graduate Student Member, IEEE), DANTI KHOURI, KONSTANTIN LOMAKIN, ANDREAS HOFMANN (Graduate Student Member, IEEE), MICHA KLEINLEIN, INGRID ULLMANN (Member, IEEE), MARTIN VOSSIEK (Fellow, IEEE), AND GERALD GOLD (Member, IEEE)

Institute of Microwaves and Photonics, Friedrich-Alexander-Universität Erlangen–Nürnberg, 91058 Erlangen, Germany

CORRESPONDING AUTHOR: L. ENGEL (e-mail: lukas.le.engel@fau.de)

This work was supported in part by the Deutsche Forschungsgemeinschaft (DFG, German Research Foundation) through GRK 2680–Project under Grant 437847244.

ABSTRACT Nowadays, additive manufacturing provides far-reaching possibilities for use in radio frequency components. In addition to almost unlimited freedom of design as compared to conventional manufacturing, the absence of further assembly steps is a key aspect of 3D printing. In this paper, a 3D printed monolithic antenna for millimeter wave-sensing applications is presented with a full hemispherical coverage. The antenna is designed as an ensemble of a waveguide horn antenna and a differentially fed dipole antenna. The slotted waveguide approach was utilized to improve the manufacturing quality on the waveguide inside. The influence of two optimized antenna elements, a metal plane, and a cut-out window, on the beam pattern is comprehensively investigated. A huge half power beam width of 142° in both directions, elevation and azimuth, is presented at 79 GHz and a boresight gain of 4.7 dBi was measured. The beam pattern in the frequency range from 76 to 81 GHz is studied in greater detail, where a half power beam width of at least 112° is achieved. Due to the −10 dB matching capability bandwidth of over 28 GHz, the antenna is also suitable for extremely broadband applications with a −5 dB angular width of better than 100°. Furthermore, the system design describes how to integrate the antenna into hybrid circuit designs and the manufacturing tolerances are examined. The antenna offers attractive possibilities for millimeter wave-sensing applications in the area of assisted living and industrial monitoring, especially whenever blind spots have to be avoided.

INDEX TERMS 3D printing, additive manufacturing, antenna, broadband, coverage, hemispherical, localization, millimeter wave, radar applications, smart home, waveguide.

I. INTRODUCTION

MILLIMETER wave (mmW) sensors will be a key enabler for technological trends, such as human machine interaction for the Internet of Things (IoT) [1], human activity recognition [2], [3], or autonomous driving [4].

While in many sensing applications at mmW frequencies high-gain antennas are required, for the above-named applications, non-directive antennas are beneficial: for indoor localization tasks in industrial halls or warehouses [5], [6], [7], [8], i.e., for robotics and navigation [9], only limited possibilities exist for mounting sensors. Therefore, it is important to permanently detect the target object with a few sensors, which requires a large coverage area. In localizing unmanned aerial vehicles (UAVs), it is important to simultaneously reach as many distributed base stations as possible to achieve high precision [10], [11]. In smart home applications, i.e., assisted living [12], [13], lighting and ventilation control and vital signs [3], [14], [15], the dimensions of the rooms are minuscule and thus a small field of view (FoV) may lead to blind spots. In security [16], [17], and medical [18], [19] applications, people are usually very close to the sensors, which means that huge FoVs are required to be able to detect and sense the entire body.

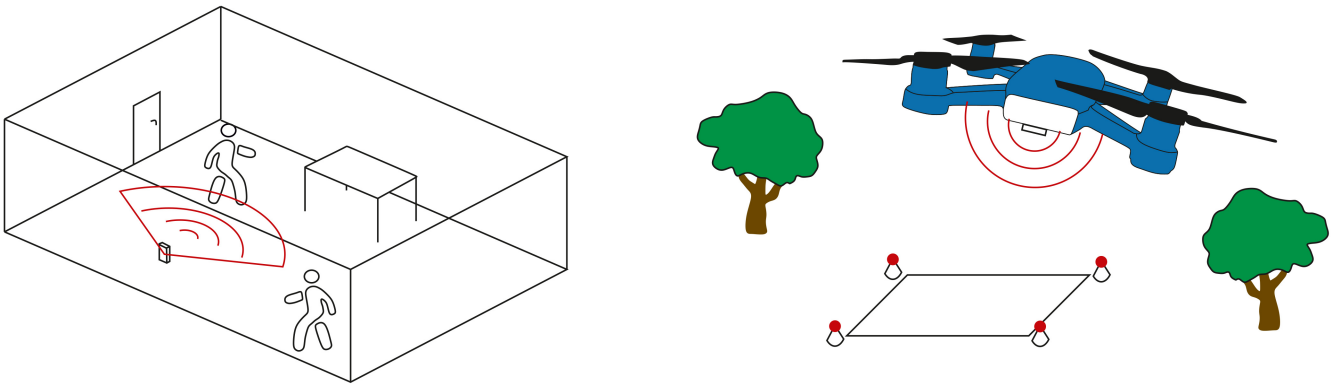

FIGURE 1. Wave-based smart home applications and controlled radar-based UAV landing process. In both scenarios, a hemispherical field of view is mandatory in order to enable detections of scatterer and reliable connections for communication.

Whereas omnidirectional antennas are desired for communication applications (e.g., Wi-Fi), hemispherical coverage is preferable for the above-mentioned applications. On the one hand, no targets of interest are expected in the backward direction and, on the other hand, strong reflectors in close neighborhood to the sensor, such as walls and car bodies, may negatively influence the measurements.

There are several approaches of antennas with a wide FoV in the literature. Many of them are in the frequency range below 10 GHz: [20] proposes a loaded monopole antenna that is folded into a few shorter sections. It shows excellent hemispherical radiation conditions. In [21], [22], [23], [24], circularly polarized antennas with hemispherical or near-isotropic coverage are presented for communication applications and GPS and [25] proposes an ultra-wide-band helical antenna. In [26], an omnidirectional crossed-loop antenna for in-band full duplex applications is presented. These antennas are manufactured by conventional machining processes. However, a mere scaling of the dimensions of these antennas to dimensions in mmW components would likely create a large susceptibility to breakage. Furthermore, several approaches exist to omnidirectional radiation patterns for communications issues. Although this is not the goal here, these approaches provide key ideas for antenna design to yield a wide beam width [27], [28], [29], [30]. Furthermore, especially at higher frequencies, printed circuit board (PCB)-based approaches [31], [32], [33], [34], [35], [36], [37], [38] exist for omnidirectional radiating antennas that show a wide coverage. However, either the dimensions of the antennas become too small for use in higher frequency ranges or the bandwidth is very limited.

Moreover, there are some 3D-printed approaches with wide coverage at a lower GHz range: In [39], a quasi-isotropic, meandered dipole antenna in the ISM frequency band was proposed. A compact monopole antenna for communication is presented in [40]. An on-package antenna was introduced in [41] and [42]. Liao et al. [43] proposes a inkjet-printed in-package antenna for marine animals monitoring and [44] suggests a dielectric resonator antenna. Furthermore, a super-wideband spidron fractal cube is

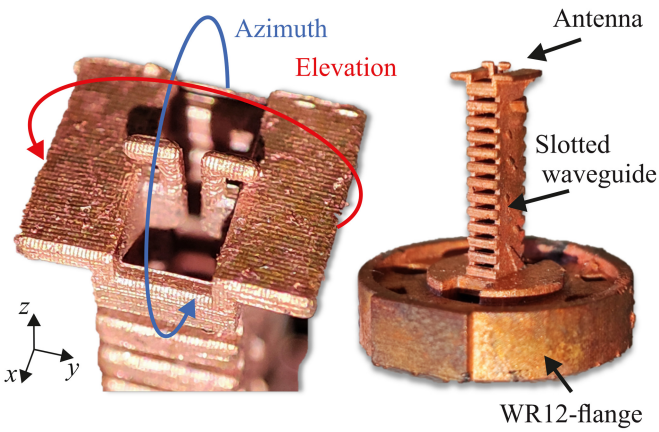

FIGURE 2. Manufactured antenna with slotted waveguide and WR12 flange in different orientations and the applied coordinate system. Two separated dipoles and the metal planes for widening the field of view can clearly be seen.

presented in [45], and a low-profile antenna for communication issues is proposed in [46]. Because of the level of detail of these antennas, it is tedious to additively manufacture them with similar precision in higher frequency ranges. A biconical antenna is presented in [47]. It is designed for 60 GHz applications, and an omnidirectional radiation pattern was achieved in the horizontal direction. However, a limited beam width in the vertical direction is present.

To the best of the authors' knowledge, there is no suitable antenna in the proposed frequency range. The existing approaches in lower frequency ranges have some shortcomings, as their manufacturing is either highly sophisticated, cost-intensive, or not easily convertible to higher frequencies. Many antennas are limited to a planar layout, although the desired antenna geometry may generally require the design freedom of all three dimensions. In some proposed approaches, manufacturing technology is fundamentally unable to provide the precision required for mmW components.

Additive manufacturing overcomes some of these shortcomings. Therefore, it is a promising alternative, as it

provides both a relatively cost-efficient machinery and manufacturing process and an inherent degree of freedom in geometry. Nowadays, stereolithography (SLA) [48] and digital light processing (DLP) [49] offer a spatial manufacturing resolution of merely several 10 µm and decent surface quality in the order of root-mean-square (RMS) surface roughness values of R_q around 1 µm and less [50], which is a decisive aspect at mmW frequencies [51], [52], [53]. Therefore, modern 3D printers have already been developed to the point enabling the high geometric precision required for mmW applications [54], [55], [56]. The printed plastic geometry is functionalized by an electroless metal coating and may be extended by electroplated surface finishes to serve as a waveguide component. Due to the skin effect, thin layers of 5 – 30 µm are absolutely enough. The slotted waveguide approach allows a high quality of metal plating on the inside of the wavguide while maintaining a monolithic structure [51].

Therefore, in this article, a novel antenna is presented that is capable of radiating in both azimuth and elevation by making use of the geometrical freedom of 3D printing. The antenna design is a mixture of a 3D printed waveguide horn antenna and a differentially fed dipole antenna. A photograph of a manufactured specimen and the applied coordinate system is given in Fig. 2.

The paper is outlined as follows: In Section II, a system design and setup are discussed as a transition from PCB to waveguide is required, which is explained in detail. Subsequently, the design of the proposed antenna is demonstrated in Section III and optimization approaches are presented in Section IV. To evaluate the manufacturing process, the dimensions of the fabricated specimen are evaluated in Section V. Moreover, the simulation and measurement results are compared and sorted according to their application in Section VI and finally concluded in Section VII.

II. SYSTEM DESIGN AND SETUP

The goal of this work is to maximize the half power beam width (HPBW) and minimize the return loss over a wide frequency range. A hemispherically radiating antenna with an HPBW of 180° in both angular directions would be the optimum. Hence, our proposed antenna was developed for a larger HPBW in both hemispherical directions. Simultaneously, a better return loss of at least −13 dB at 79 GHz compared to an open waveguide antenna should be achieved. Nowadays, PCB technology is the most utilized assembly method. It allows for an integration of both passive and active RF components. However, enormous losses are expected at higher frequencies in microstrip transmission lines. To overcome this major drawback of PCB technology, hybrid systems provide a remedy. A waveguide technique addressing low losses and inherent shielding is the use of hollow waveguides that can easily be attached on top of the PCB. Therefore, high-performance transitions from waveguides to PCB-based transmission lines are necessary.

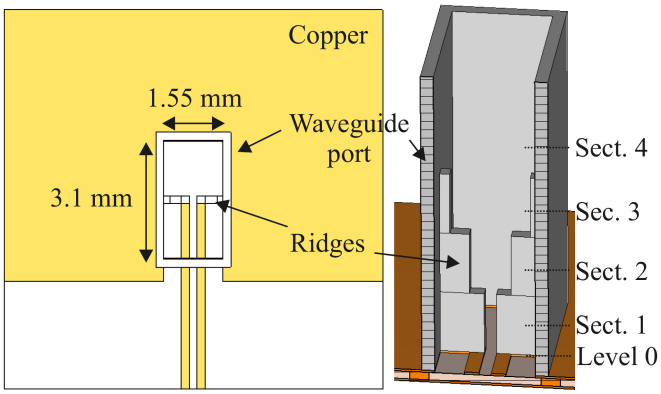

FIGURE 3. Top and side views of the waveguide to PCB transition.

State-of-the-art active radar components mainly provide differential signaling as an output. Therefore, a performant transition from PCB to waveguides is required. The design of a suitable differential transition is shown in Fig. 3, which is presented in detail in [57] or in [58] as a more broadband alternative. Its functional principle and additional design aspects are given in [59]. Measurements state a return loss of $|s_{11}|^2 < -24$ dB and an insertion loss $|s_{21}|^2$ better than −1.3 dB at 77 GHz for the transition. This demonstrates excellent suitability for hybrid circuits. Since the transition of the PCB to the waveguide is quite similar to the transition from the waveguide to the proposed antenna, the general functionality will be further explained in detail.

The transition has two symmetry planes in both halves: the broad side and the narrow side of the waveguide. The electric field of the TE_{10} mode is maximal at the center of the broadside of the waveguide. Two ridges on each sidewall are directly located at the maximum of the electric field, so that the electric field is concentrated between the ridges. Therefore, a stepwise conversion of the TE_{10} mode to the guided differential microstrip line (DMSL) mode is performed. The height of the individual ridges is designed to be about a quarter of the waveguide wavelength to minimize reflections. The waveguide body is placed on the DMSL in such a manner that the ridges at the bottom of the waveguide and the DMSL coincide. The width and depth of the ridges and the DMSL have exactly the same dimensions at their intersection interfaces. To avoid leakage effects into the substrate, a via fence on the PCB is applied where the waveguide contour confines the footprint.

At the center of the broad side of the waveguide, the DMSL is angled toward the side walls of the waveguide. To cause the maximum of the electric field between the two differential lines at the gap of the connection of the ridges, the length of the short inset part is chosen as a quarter of the wavelength of the PCBs differential microstrip mode. Due to the via fence in the plane, the short inset part acts as a shorted stub. The width of the ridge t_0, close to the bottom, is defined by the width of inset t. It is a trade-off between field matching and fabrication capabilities.

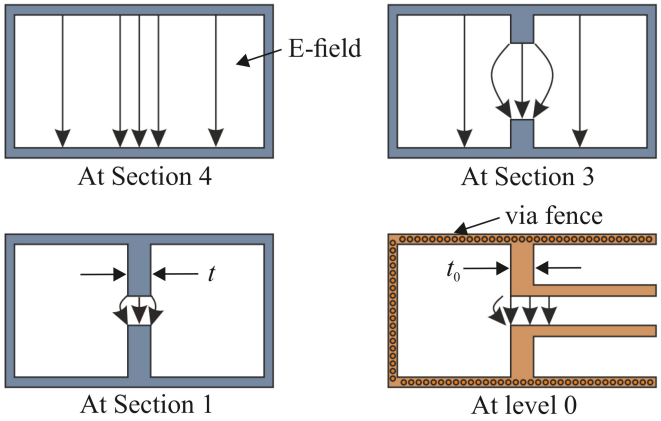

FIGURE 4. Conversion of the TE_{10}-mode to the differential microstrip mode in different cross-sections in relation to Fig. 3.

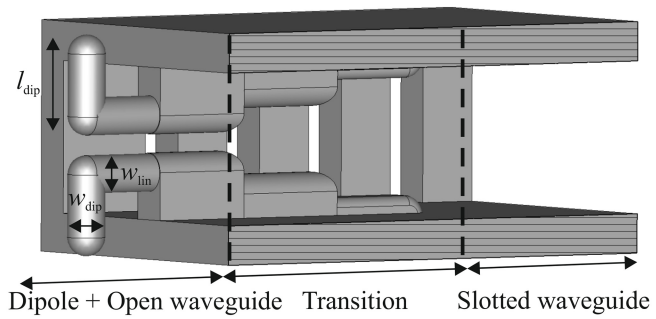

FIGURE 5. Developed waveguide antenna with the transition from the slotted waveguide to the radiating part via the ridged transition.

The mode conversion of the TE_{10} mode to the DMSL mode is shown in Fig. 4. Here, stepwise mode conversion is shown in several sections. The upper left picture shows the distribution of the electric field mode TE_{10} in a rectangular waveguide. By inserting the ridges on the broadside walls of the waveguide, the field distribution can also be exploited as a differential feed for linear dipole antennas, as can be seen in the bottom left scheme in Fig. 4.

III. PROPOSED ANTENNA DESIGN

In this section, the design of the proposed antenna is presented. The antenna comprises three parts: the slotted waveguide part, the mode transition part with cascade ridges, and the actual radiating part that is an ensemble of an optimized differential fed dipole antenna and an open waveguide antenna formed by a standard E-band waveguide. All three parts are depicted in Fig. 5. In the following sections, the functionality of the individual elements is addressed.

A. SLOTTED WAVEGUIDE

The waveguide connects the PCB transition to the radiating antenna and serves as a transmission line. This enables the antenna to be integrated into even complex arrays, where the alignment of the feed structures on the PCB becomes relatively independent from the placement of the antennas. Considering the fact that the overall losses in the slotted waveguide feed are typically one or more magnitudes less than those on PCB-based transmission lines, feeding even large arrays becomes feasible. An arbitrary arrangement, especially toward $\lambda/2$ in all directions, is quite challenging. However, this is also the case with many other antenna types, such as horn antennas or slotted waveguide array antennas. In comparison to the latter, the proposed antenna offers a significant advantage in terms of compactness. The slotted waveguide differs from a continuous waveguide in that it removes some parts of the narrow side wall of the waveguide. Since surface current components located on the narrow sidewalls are oriented top down, the field mode is affected insignificantly by the removed parts of the side wall. Furthermore, no waveguide slot antenna is created here because the surface current is mainly parallel to the slot shape. Here, the slotted waveguide approach is utilized for the sake of printing quality and metal plating. The length and height of the slots is an optimum of manufacturing and electrical properties and is studied in detail in [55].

B. WAVEGUIDE MODE TRANSITION AND INTERFACE TO RADIATING PART

The transition of the waveguide to the antenna works according to a similar principle as the transition from the PCB to the waveguide. Symmetrical ridges are used for impedance matching and concentrating the electrical field between them. Thereby, a differential feed of the antenna is provided as a source for the antenna at the edge of the waveguide. The resulting source mode excitation is depicted in the bottom left drawing in Fig. 4.

C. RADIATING PART

The radiating part is an interaction of following two components: the differential fed dipole antenna and the open waveguide. In general, dipole antennas are characterized by an omnidirectional radiation pattern in the azimuth due to their rotational symmetry. However, the beam pattern in elevation is highly dependent on the length of the dipole. Dipoles longer than the wavelength develop undesired side lobes. This results in zero of the beam pattern, which is explicitly not the goal of the proposed antenna. However, dipoles smaller than the wavelength do not exhibit any zeros. In general, shorter dipoles have a larger HPBW in their respective directions [60]. Therefore, a dipole shorter than a wavelength is beneficial as the radiating part of this antenna. In the proposed antenna, the dimensions of one dipole element are chosen to be about 1 mm in height l_{dip} and around 400 µm in width w_{dip}. The exact height and width of the dipoles are optimized for impedance matching and angular width in CST's Microwave Studio. For printability reasons and impedance matching, the caps at the end of the dipoles are rounded. The distance between dipoles and the edge of the waveguide is crucial for the pattern and also optimized for this application.

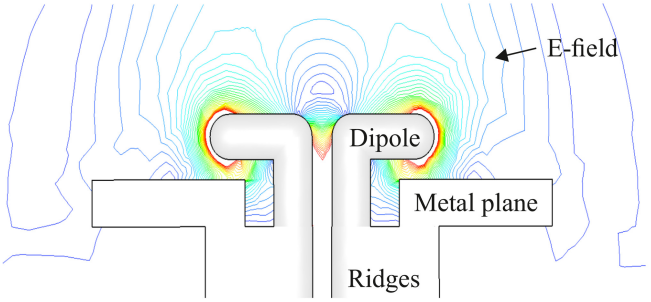

FIGURE 6. Electrical field distortion due to metal planes. Due to the metal plane, significantly more power radiates in the direction of the metal surface.

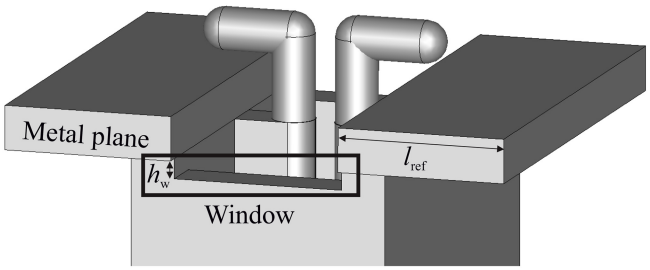

FIGURE 7. The proposed hemispherically radiating antenna with a small window and metal planes to improve the angular width.

IV. OPTIMIZATION OF THE RADIATION PATTERN

Based on the design in Fig. 5, some further optimization steps are investigated and conducted to increase the angular width of the antenna. Two main approaches exist to enhance the beam pattern of this antenna. On the one hand, a metal plane in the x–y-plane is inserted on the broadside wall at the edge of the waveguide. On the other hand, a cutting window on the narrow side wall at the edge of the waveguide is incorporated into the design.

The metal plane has a significant positive influence on the beam pattern. The metal planes affect the electric field in such a way that remarkably more power is radiated along the metal plane's surfaces as presented in Fig. 6. The width of the metal planes was identical to the overall dimensions of the waveguide in the broadside direction. Beyond it, a small window is cut out on the narrow side of the waveguide. In particular, the HPBW in the azimuth is increased even further as a result. The optimized final antenna is depicted in Fig. 7.

Additional simulations were performed to further investigate the effect of the length of the metal plane l_{ref} on beam patterns. The simulated beam patterns in the azimuth and elevation at 79 GHz are presented in Fig. 8 and Fig. 9, respectively. If l_{ref} equals 0, no metal plane is present, which leads to a narrow beam pattern similar to an open waveguide antenna. However, by increasing the length of the metal plane up to a certain length, the HPBW in both directions azimuth and elevation rises. As the length of the metal plane exceeds the optimum of 1.535 mm, the HPBW shrinks.

Furthermore, the influence of the height of the window h_w was examined. In Fig. 10 and Fig. 11 the beam patterns

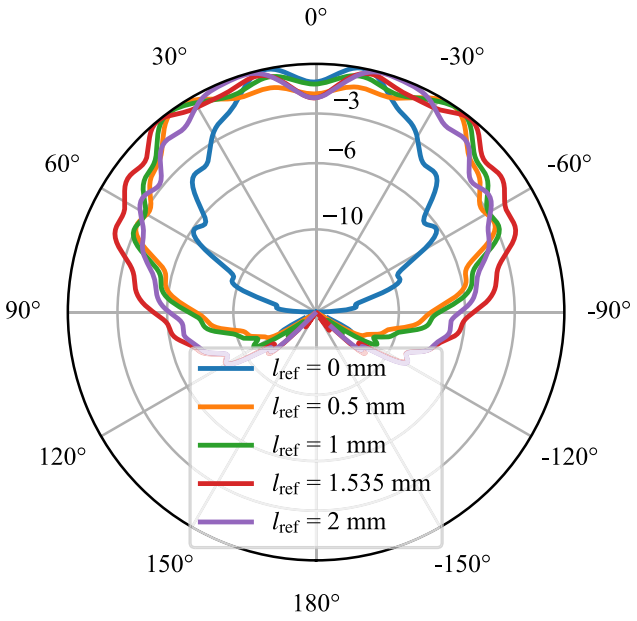

FIGURE 8. Simulated and normalized beam patterns at 79 GHz in the azimuth direction in decibel. The simulations differed in the value of the length of the metal plane l_{ref}.

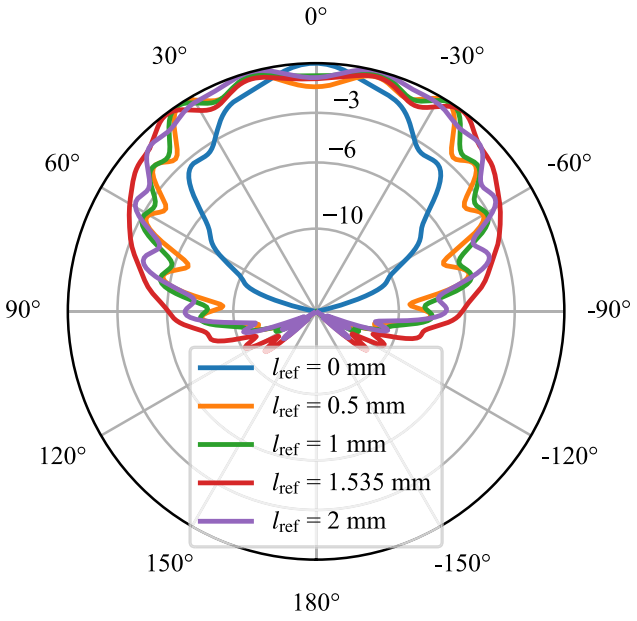

FIGURE 9. Simulated and normalized beam patterns at 79 GHz in the elevation direction in decibel. The simulations differed in the value of the length of the metal plane l_{ref}.

in azimuth and elevation at 79 GHz dependent on the height of the window are depicted. Apparently, the height of the window has little influence on the beam patterns in elevation. Further improvements in the HPBW in the azimuth can be achieved. Here, the HPBW rises by increasing the height of the window. However, significant ripples emerge in the beam pattern, especially at the boresight of the antenna at an angle of $\vartheta = \phi = 0$. To ensure the uniformity of radiation of power toward all angles of the hemisphere, a compromise

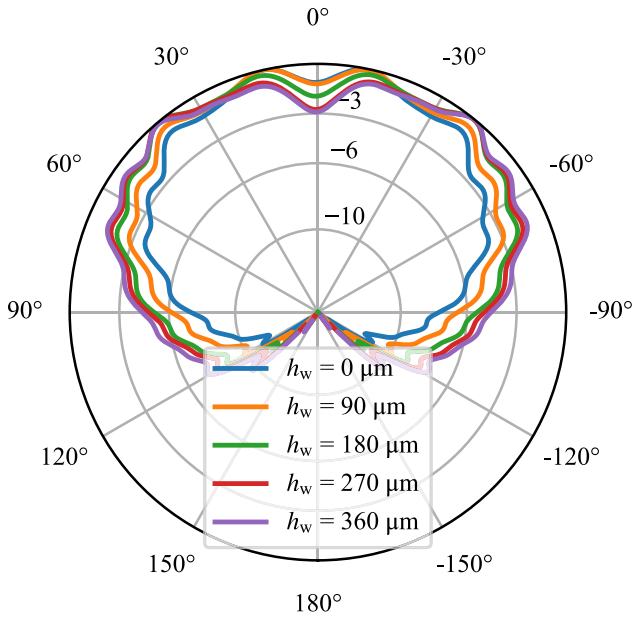

FIGURE 10. Simulated and normalized beam patterns at 79 GHz in the azimuth direction in decibel. The simulations differed in the value of the height of the window h_w.

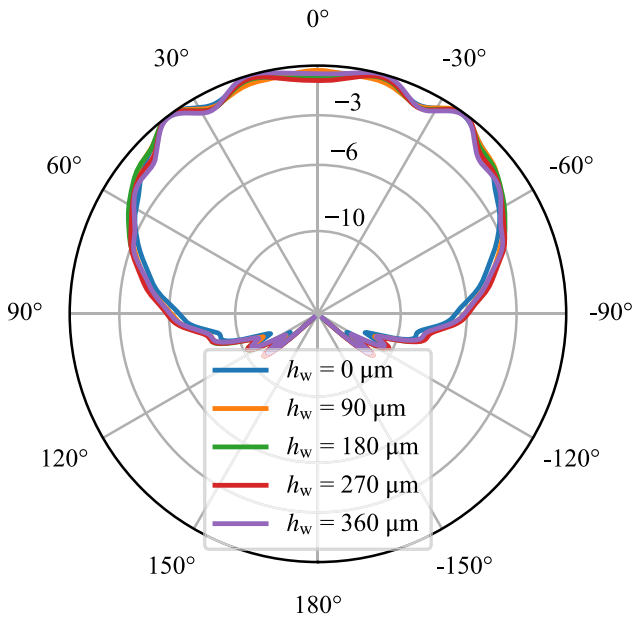

FIGURE 11. Simulated and normalized beam patterns at 79 GHz in the elevation direction in decibel. The simulations differed in the value of the height of the window h_w.

between HPBW and ripples is required. For this purpose, the height of the window h_w is chosen to be 180 µm. Overall, by inserting these parts, the HPBW is increased by more than 50° in both azimuth and elevation direction.

V. MANUFACTURING PROCESS

The base body of the antenna is fabricated using additive manufacturing. The fabrication process is described in detail in [55]. First, a polymer body of the antenna is fabricated by

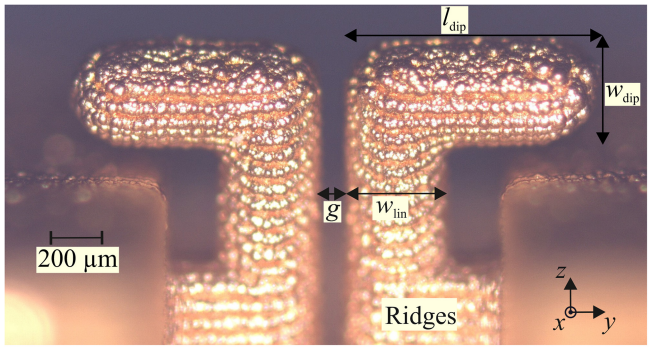

FIGURE 12. Close-up side-view image of the inner part of the antenna. The dipoles are clearly separated and fully covered with a metal surface.

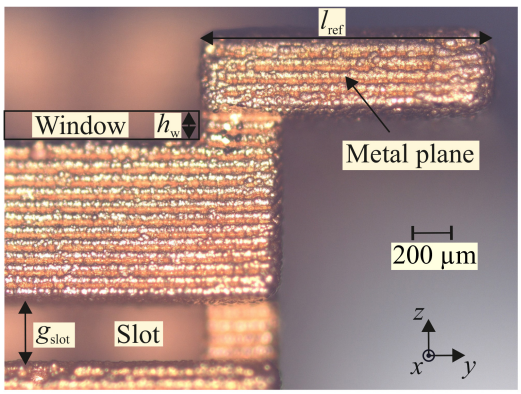

FIGURE 13. Close-up side-view image of the upper antenna part with the manufactured metal plane and the slotted waveguide.

SLA printing using UV sensitive resin. Afterwards, it is cured in an UV chamber with accurate time profiles. Subsequently, a conductive silver layer is applied to the surfaces of the printed antenna by an electroless plating process and finally galvanized with copper. The thickness of the materialization is usually several skin depths to ensure that the photopolymer no longer interacts with the electromagnetic wave. With this process, a conductivity σ_{DC} of better than 30 MS/m and an effective RMS-surface roughness of $R_q < 800$ nm can be achieved which is a decisive parameter for incorporating losses at frequencies in mmW range. This results in overall losses better than 10 dB/m [55], [61].

A photograph of antenna specimens are depicted in Fig. 2. On the left-hand side, a close-up image of the dipoles and metal planes is shown. One can clearly see the separated dipoles at the interface with the respective ridges. Furthermore, the metal planes on both broad wall sides and the window are clearly recognizable. On the right-hand side, the antenna with a 10 mm long slotted waveguide is depicted. To measure the characteristics of the antenna, a standard WR12 waveguide flange is attached to the lower part.

A. EVALUATION OF MANUFACTURING PROCESS

In Fig. 12, a side-view photograph using a Keyence microscope of the inner part of the radiating section of the antenna is depicted. One can clearly identify two fairly symmetrical

TABLE 1. Dimensions of the antenna.

Dimensions in µm	l_{dip}	w_{dip}	w_{lin}	g	g_{slot}	l_{ref}	h_{w}
Simulation	1025	386	386	201	400	1535	180
Measurement	1084	444	430	122	386	1571	161
Difference	59	58	44	79	14	36	19
Mean deviation to simulation*	32.3	59.8	42.3	74	n.a.	23.6	24.5
Mean deviation within specimen*	15.0	16.6	11.2	15.8	n.a.	15.3	12

*Deviations of eight fabricated specimen.
n.a.: not acquired

dipole elements attached to the ridges in the center of the waveguide. The gap between the two dipoles shows a straight course, and the dipoles and the caps of the dipoles are evenly rounded.

A side-view photograph of the outer part of the antenna is shown in Fig. 13. One side of the metal plane and a fraction of the slotted waveguide are depicted. Even though the metal plane represents a challenge for 3D printing due to the large overhang in the model, it is printed extremely straight. Furthermore, the small window at the narrow side of the waveguide for optimizing the beam pattern is clearly visible. The images of the specimen clearly illustrate the horizontal layer-by-layer structure due to the printing process.

The dimensions of the manufactured specimens are given in Table 1. The measured dimensions generally agree well with the simulation. The precision in the z-direction stays clearly below a difference of 36 µm, whereas the dimensions of the dipole are roughly two times larger due to the printing direction. Furthermore, the mean deviations of eight fabricated specimens are compared to simulation and measurement. The mean deviation to the simulation is in the order of the difference between the simulation and the measurement of the proposed antenna, whereas the order of magnitude of the mean deviations within various specimen is much smaller. As the deviations cause only moderate degradation of the performance of the antenna, the design can potentially be adapted to compensate for the manufacturing tolerances. Nevertheless, this results in a precision that is sufficient for mmW components.

VI. SIMULATION AND MEASUREMENT RESULTS

Measurements were performed using a VNA (ZVA50) from Rohde&Schwarz with mmW-extensions for E-band (WR12). To improve measurement precision, a Trough-Open-Short-Match (TOSM) waveguide standard algorithm was applied at the interface of the antenna's flange and the Test Port Adapter.

Fig. 14 shows the measurement and simulation results for the reflection coefficient $|s_{11}|^2$ of the antenna in a frequency range from 60 to 90 GHz. Comparing the simulation with and without the waveguide flange, the trend

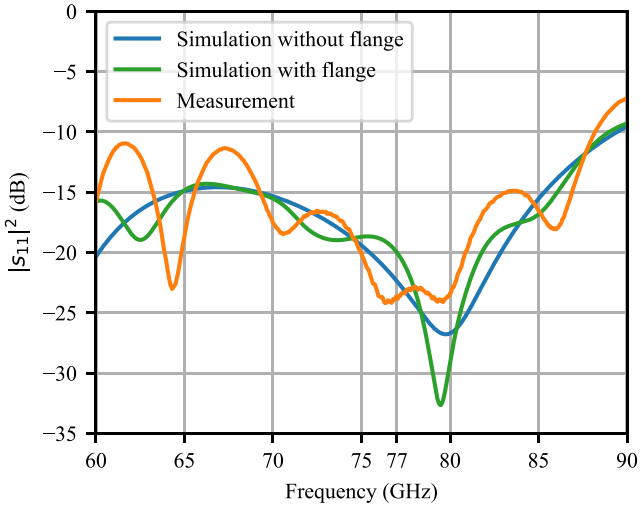

FIGURE 14. Simulated and measured reflection coefficient of the antenna.

remains the same, but small ripples occur. Moreover, the trend of the response of the measured parameter $|s_{11}|^2$ agrees well with the simulation. It shows an excellent matching of −20 dB in the region of 75 - 81 GHz and stays below −10 dB over the frequency range of E-band up to 88 GHz. The −15 dB bandwidth equals 14 GHz. Deviations from simulation and measurement could originate from manufacturing tolerances of the model, and additional ripples are probably caused by line resonance effects of the slotted waveguide part, or due to interface mismatches of the antenna flange and the Test Port Adapter. Due to the resonant structure of the dipole, a dip at 80 GHz occurs, while far away from the resonance, the matching characteristic of an open waveguide is achieved. Due to the slight increase in dipole length, the measurement is slightly shifted to smaller frequencies compared to the simulation. These results highlight the promising possibilities of additive manufacturing in the mmW range, even for complex geometric models, and, due to the inherent very broadband design of the proposed structure, the shift in frequency is absolutely within the bandwidth-budget.

The simulated efficiency over frequency of the antenna is depicted in Fig. 15. A parameter sweep of the conductivity σ_{DC} and the surface roughness R_{q} was performed. Whereas the conductivity has only a medium influence on the efficiency, the surface roughness has strong influence on the antenna efficiency at mmW frequencies. The trend of the efficiency clearly shows the inverted trend of the simulated reflection coefficient with flange in Fig. 14, which is likely to be the main cause of the efficiency drop. For a surface roughness of 0.8 µm and a conductivity of 30 MS/m, an efficiency of 96% at 79 GHz can be achieved, which means that only 4% of the stimulated power is not radiated. Even at a conservative estimate ($\sigma_{\mathrm{DC}} = 20$ MS/m, $R_{\mathrm{q}} = 1.2$ µm), the efficiency of the antenna stays above 90% in over 85% of the E-band frequency range, which indicates the high efficiency of waveguide antennas.

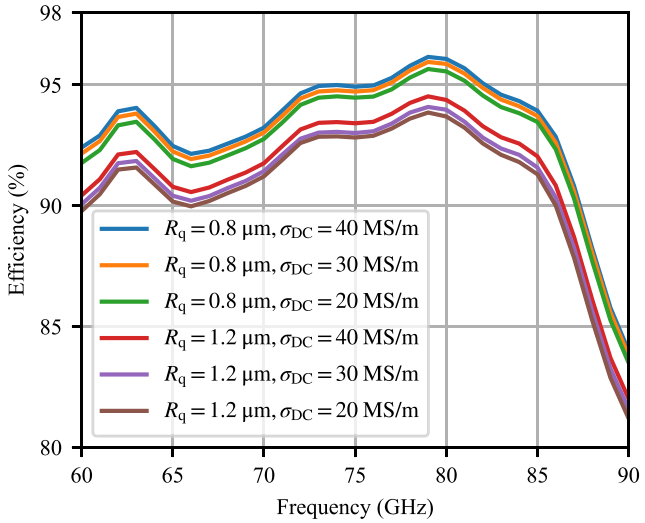

FIGURE 15. Simulated efficiency of the antenna dependent on the conductivity σ_{DC} and the surface roughness R_q.

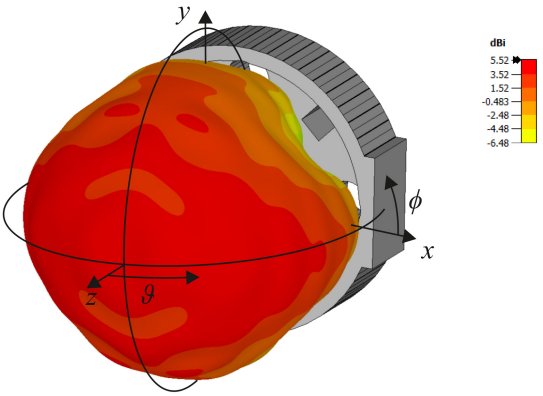

FIGURE 16. 3D farfield simulation of the proposed antenna with hemispherical coverage.

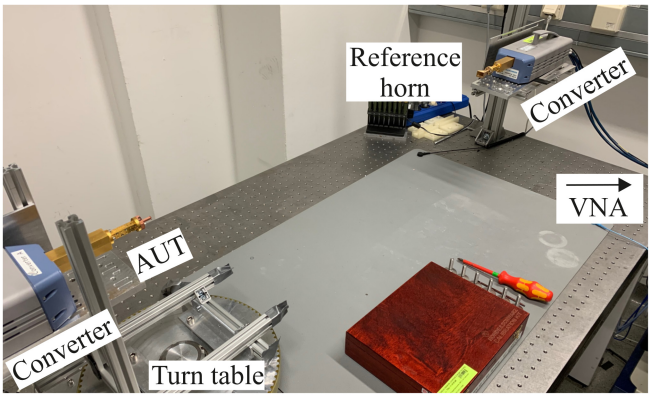

FIGURE 17. Measurement setup: The AUT was mounted on a turn-table to measure the beam patterns. The AUT- and the reference horn antenna were connected to a VNA via E-band converters.

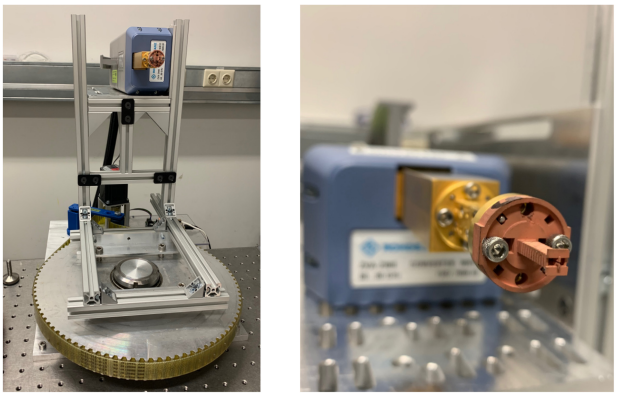

FIGURE 18. Measurement setup: Single-axis turn table (left) and proposed antenna specimen mounted on the Test Port Adapter (right).

A 3D farfield simulation of the proposed antenna is depicted in Fig. 16. For the sake of orientation, the waveguide flange of the antenna can clearly be seen in the background. The radiating parts of the antenna are built in positive z-direction. The antenna's 3D farfield beam pattern shows a full coverage of the hemisphere. The simulated pattern states in azimuth direction ($\phi = 0°$) and elevation direction ($\phi = 90°$) a wide HPBW of 146° and 136°, respectively. The section plane at $\phi = 45°$ is the most critical plane, with an HPBW still better than 110° and a −5 dB angular width of 137°, which is absolutely sufficient for most of the applications.

Measurements were carried out to obtain the beam pattern of the manufactured antenna using the setup as shown in Fig. 17 and Fig. 18, respectively. A 21 dBi standard-gain horn antenna [62] was used as a reference for the measurements and placed at a distance of about 1 m from the antenna under test. A single axis turntable setup, as shown in Fig. 18 was used to characterize the antenna's beam pattern by scanning one hemispherical axis from −100° to 100° in 2° steps. To measure both elevation and azimuth, the antenna under test and the reference antenna are rotated by 90° around the main lobe axis.

The simulated and measured boresight gain ($\vartheta = \phi = 0°$) over frequency is shown in Fig. 19. The trend of the measured gain agrees with the simulation; however, an offset occurs. A boresight gain of 4.7 dBi was measured at a frequency of 79 GHz. A higher gain in the measurement than in the simulation seems counterintuitive. However, it is noteworthy that a measured gain at boresight direction only implies less radiation in other angular directions, which means that the antenna is more directive in a frequency range below 80 GHz than expected.

The simulated and measured beam patterns in azimuth at 79 GHz are presented in Fig. 20. The measurement results agree very well with the simulation. The standard deviation from measurement to simulation is 0.52 dB. A remarkable HPBW of 142° is achieved and the −5 dB angular width at 79 GHz is even about 180°. Thus, the antenna clearly meets the desired coverage in azimuth. The simulated and measured beam patterns in elevation at 79 GHz are depicted in Fig. 21. In this direction, the standard deviation from measurement to simulation is 0.97 dB. A HPBW of 142° is achieved, and

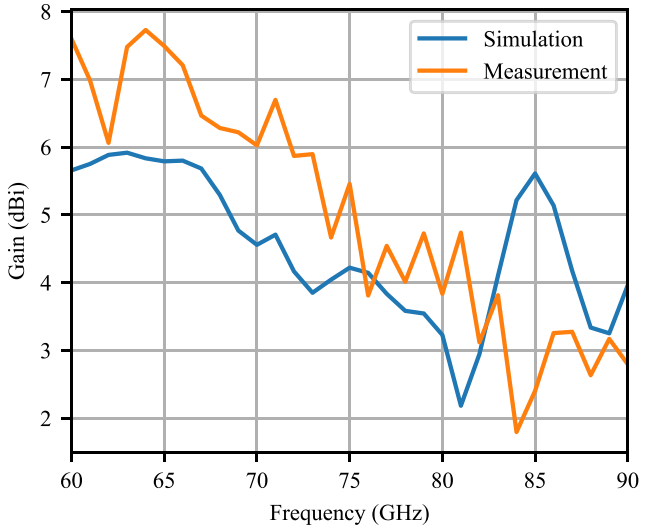

FIGURE 19. Simulated and measured boresight gain over frequency.

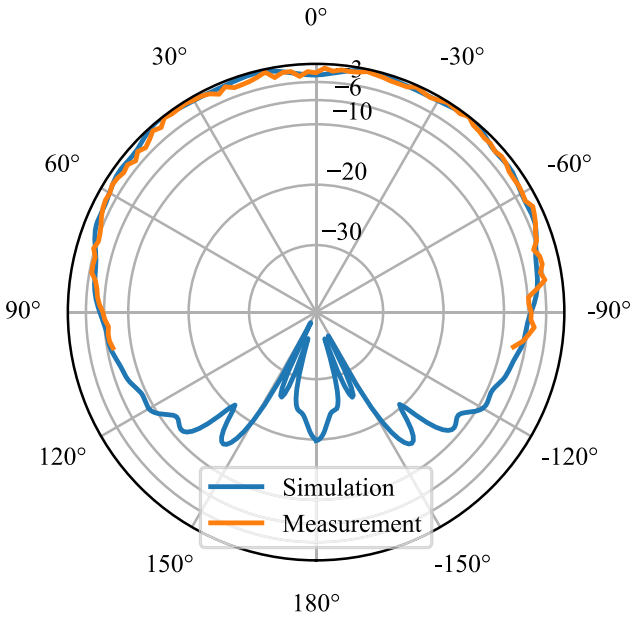

FIGURE 20. Simulated and measured normalized beam patterns at 79 GHz in decibel in the azimuth direction.

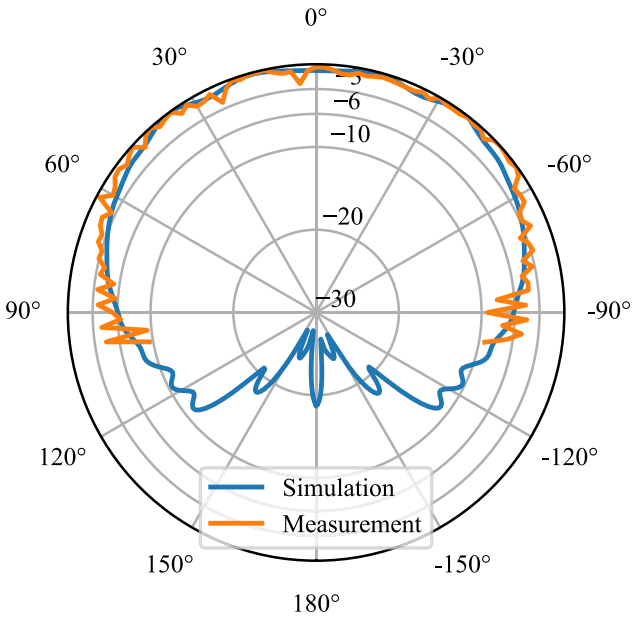

FIGURE 21. Simulated and measured normalized beam patterns at 79 GHz in decibel in the elevation direction.

the 5 dB angular width at 79 GHz is 166°. Due to the large angular width simultaneously in both elevation and azimuth, the antenna has excellent coverage of the entire hemisphere.

A. MEASUREMENT RESULTS IN FREQUENCY RANGE 76 - 81 GHz

In this section, the characteristics of the antenna is considered in more detail in the frequency range from 76 - 81 GHz. For this reason, the HPBW and the beam patterns for these specific frequencies are presented.

In Fig. 22, the measured beam patterns of the antenna in the azimuth are depicted. The beam patterns show a good illumination of the scenery over the entire frequency range. The maximum difference in the beam patterns of the displayed frequencies is less than 2 dB in the angular range from −60° to 60° and stays below 3.6 dB for the entire azimuth axis for the hemisphere. In elevation, the measured radiation patterns of all the depicted frequencies show a large angular width but with a slightly larger variance than in azimuth. However, the maximum difference in the beam patterns of the displayed frequencies is less than 3.1 dB in the angular range from −60 to 60° and stays below 4.5 dB for the entire elevation axis in the hemisphere.

The measured HPBW of the antenna is depicted in Fig. 24 in the frequency range from 75 to 82 GHz. The HPBW in azimuth is always slightly larger than that in elevation and stays above 137°. However, the HPBW in elevation also exhibits a huge angular range and has an angular width larger than at least 112°. These measurements state its excellent applicability to radars in the 79 GHz range, which are explicitly designed for large FoVs.

B. MEASUREMENT RESULTS FOR BROADBAND APPLICATIONS

In many measurement setups, utilizing a wide bandwidth is crucial for the performance of the system as well as for the received power. In particular, in measurement setups with phase-based processing and coherently processed data from different view angles, it seems sufficient to consider the −5 dB angular width instead of the HPBW as long as a large measurement bandwidth is available. It should be noted that only those angular ranges are designated as HPBW, at which the beam pattern falls below the difference from the maximum to −3 dB for the first time. However, at some frequency points, the power falls below −3 dB at only one small angle range, but at the following adjacent angle range, more than

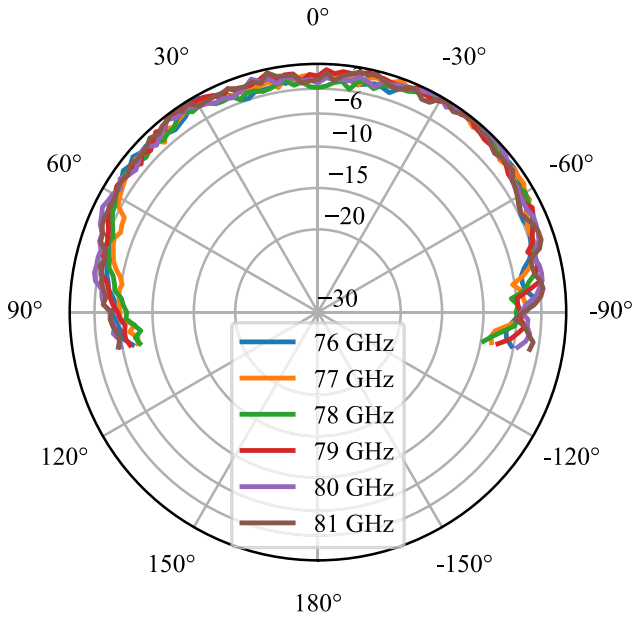

FIGURE 22. Simulated and measured normalized beam patterns at specific frequencies in decibel in the azimuth direction.

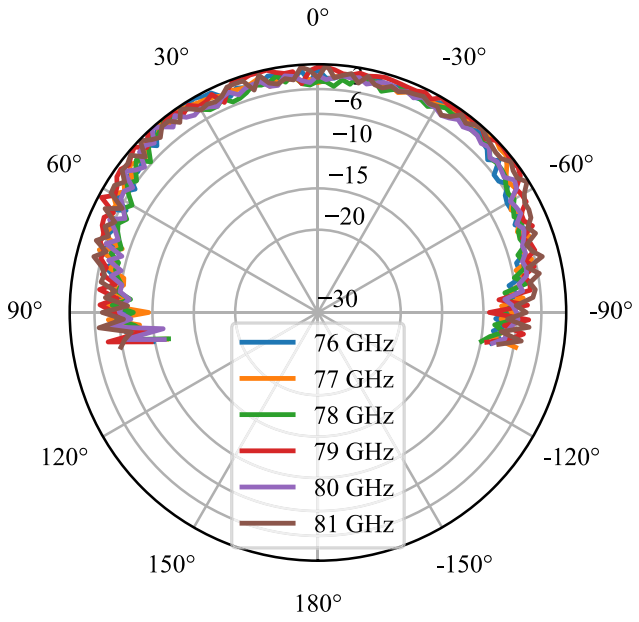

FIGURE 23. Simulated and measured normalized beam patterns at specific frequencies in decibel in the elevation direction.

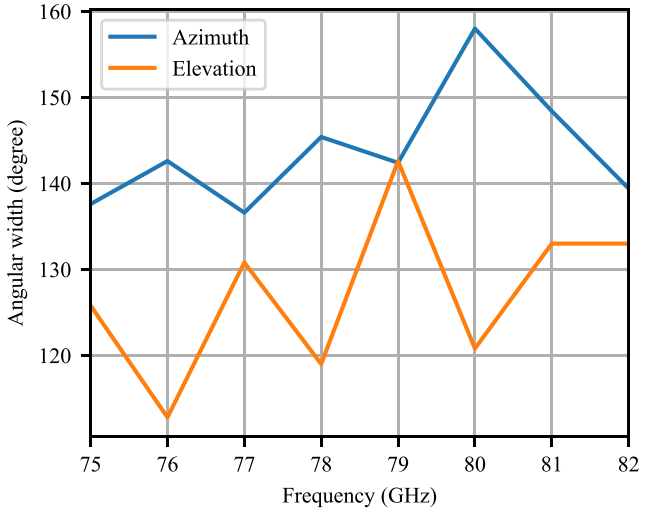

FIGURE 24. Measured half-power beam width over frequency of the antenna in the azimuth and elevation direction.

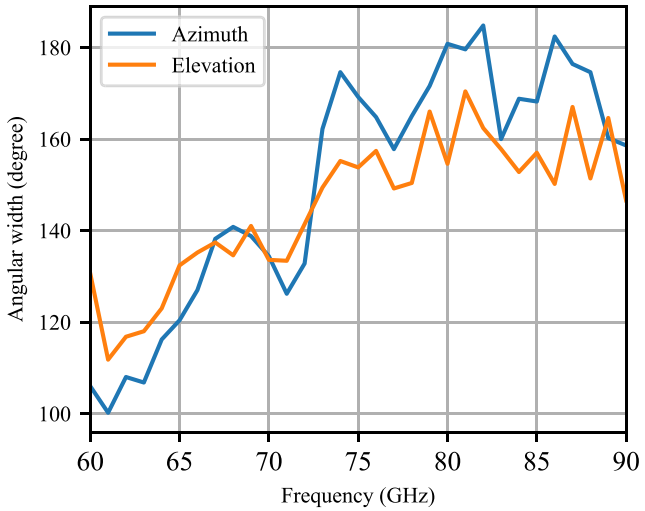

FIGURE 25. Angular width (−5 dB) over frequency of the antenna in the azimuth and elevation direction.

−3 dB power is radiated. For practical applications, this dip in a very limited angular range is often indecisive. For this reason, the −5 dB angular width is now used here to neglect small dropouts; however, it still takes sufficient power into account.

Since the antenna shows a usable bandwidth almost over the entire E-band, the angular width (−5 dB) of the antenna for 60-90 GHz is depicted in Fig. 25. The measurement results indicate a decrease of the angular width toward smaller frequencies but stays above 100° for both the angular width in elevation and azimuth. In a frequency range from 73 to 90 GHz, even an angular width of more than 140° can be observed. At 79 GHz, an angular width of 172° could be achieved, and at 82 GHz, more than 180° are measured.

VII. CONCLUSION

In this work, an additively manufactured hemispherically radiating antenna is presented. Whereas, on average, the manufacturing tolerances deviate from the simulation by a maximum of 74 µm, the mean deviation of the manufacturing tolerances within the specimens is significantly smaller. Here, a maximum mean deviation of only 17 µm was measured. Therefore, the design is can potentially be adapted to compensate for the manufacturing tolerances. The tolerances are likely to be the main source of deviations between simulation results and measurement evaluations. However, these deviations result in an only moderate degradation of

the antenna's performance, leading to a robust manufacturing process. The results demonstrate the fundamental suitability of this technology for mmW applications. The special feature of the proposed antenna is its remarkably large angular width combined with a large usable bandwidth for broadband applications. A HPBW of 142° in both elevation and azimuth at 79 GHz demonstrate an excellent coverage of the hemisphere. In addition, a usable bandwidth of more than 28 GHz enables broadband applications and encourages the applicability of the antenna in applications where a large field of view is required.

ACKNOWLEDGMENT

The authors thank Golden Devices GmbH for assisting in the manufacturing process.

REFERENCES

[1] M. U. Farooq, M. Waseem, S. Mazhar, A. Khairi, and T. Kamal, "A review on Internet of Things (IoT)," *Int. J. Comput. Appl.*, vol. 113, no. 1, pp. 1–7, Mar. 2015. [Online]. Available: http://research.ijcaonline.org/volume113/number1/pxc3901571.pdf

[2] X. Li, Y. He, and X. Jing, "A survey of deep learning-based human activity recognition in radar," *Remote Sens.*, vol. 11, no. 9, p. 1068, May 2019. [Online]. Available: https://www.mdpi.com/2072-4292/11/9/1068

[3] S. Z. Gurbuz and M. G. Amin, "Radar-based human-motion recognition with deep learning: Promising applications for indoor monitoring," *IEEE Signal Process. Mag.*, vol. 36, no. 4, pp. 16–28, Jul. 2019. [Online]. Available: https://ieeexplore.ieee.org/document/8746862/

[4] C. Waldschmidt, J. Hasch, and W. Menzel, "Automotive radar—From first efforts to future systems," *IEEE J. Microw.*, vol. 1, no. 1, pp. 135–148, Jan. 2021.

[5] F. Zafari, A. Gkelias, and K. Leung, "A survey of indoor localization systems and technologies," Jan. 2019, *arXiv:1709.01015*.

[6] P. Gulden, S. Roehr, and M. Christmann, "An overview of wireless local positioning system configurations," in *Proc. IEEE MTT-S Int. Microw. Workshop Wireless Sens. Local Position., RFID*, Sep. 2009, pp. 1–4. [Online]. Available: http://ieeexplore.ieee.org/document/5307894/

[7] M. Vossiek, L. Wiebking, P. Gulden, J. Wieghardt, C. Hoffmann, and P. Heide, "Wireless local positioning," *IEEE Microw. Mag.*, vol. 4, no. 4, pp. 77–86, Dec. 2003. [Online]. Available: http://ieeexplore.ieee.org/document/1266069/

[8] M. Lipka, E. Sippel, and M. Vossiek, "An extended Kalman filter for direct, real-time, phase-based high precision indoor localization," *IEEE Access*, vol. 7, pp. 25288–25297, 2019. [Online]. Available: https://ieeexplore.ieee.org/document/8648434/

[9] Y. Dobrev, M. Vossiek, M. Christmann, I. Bilous, and P. Gulden, "Steady delivery: Wireless local positioning systems for tracking and autonomous navigation of transport vehicles and mobile robots," *IEEE Microw. Mag.*, vol. 18, no. 6, pp. 26–37, Sep./Oct. 2017. [Online]. Available: http://ieeexplore.ieee.org/document/8003614/

[10] Y. Dobrev et al., "Radar-based high-accuracy 3D localization of UAVs for landing in GNSS-denied environments," in *Proc. IEEE MTT-S Int. Conf. Microw. Intell. Mobility (ICMIM)*, Apr. 2018, pp. 1–4.

[11] T. Pavlenko, M. Schütz, M. Vossiek, T. Walter, and S. Montenegro, "Wireless local positioning system for controlled UAV landing in GNSS-denied environment," in *Proc. IEEE 5th Int. Workshop Metrol. AeroSpace (MetroAeroSpace)*, Jun. 2019, pp. 171–175.

[12] Y. Kim, I. Alnujaim, and D. Oh, "Human activity classification based on point clouds measured by millimeter wave MIMO radar with deep recurrent neural networks," *IEEE Sensors J.*, vol. 21, no. 12, pp. 13522–13529, Jun. 2021.

[13] K. Hanifi and M. E. Karsligil, "Elderly fall detection with vital signs monitoring using CW doppler radar," *IEEE Sensors J.*, vol. 21, no. 15, pp. 16969–16978, Aug. 2021. [Online]. Available: https://ieeexplore.ieee.org/document/9429253/

[14] B. R. Upadhyay, A. B. Baral, and M. Torlak, "Vital sign detection via angular and range measurements with mmWave MIMO radars: Algorithms and trials," *IEEE Access*, vol. 10, pp. 106017–106032, 2022.

[15] Y. Hu and T. Toda, "Remote vital signs measurement of indoor walking persons using mm-Wave FMCW radar," *IEEE Access*, vol. 10, pp. 78219–78230, 2022. [Online]. Available: https://ieeexplore.ieee.org/document/9839588/

[16] S. S. Ahmed, "Microwave imaging in security—Two decades of innovation," *IEEE J. Microw.*, vol. 1, no. 1, pp. 191–201, Jan. 2021. [Online]. Available: https://ieeexplore.ieee.org/document/9318765/

[17] K. Root, J. Adametz, F. Gumbmann, I. Ullmann, and M. Vossiek, "Improved threat detection in walk-through security scanning using an optimized polarimetric target decomposition method," *IEEE J. Microw.*, vol. 3, no. 1, pp. 16–28, Jan. 2023.

[18] D. Wang, J. Park, H.-J. Kim, K. Lee, and S. H. Cho, "Noncontact extraction of biomechanical parameters in gait analysis using a multi-input and multi-output radar sensor," *IEEE Access*, vol. 9, pp. 138496–138508, 2021.

[19] H. Abedi, J. Boger, P. P. Morita, A. Wong, and G. Shaker, "Hallway gait monitoring using novel radar signal processing and unsupervised learning," *IEEE Sensors J.*, vol. 22, no. 15, pp. 15133–15145, Aug. 2022.

[20] E. Altshuler and D. Linden, "Design of a loaded monopole having hemispherical coverage using a genetic algorithm," *IEEE Trans. Antennas Propag.*, vol. 45, no. 1, pp. 1–4, Jan. 1997.

[21] C. Deng, Y. Li, Z. Zhang, and Z. Feng, "A circularly polarized pattern diversity antenna for hemispherical coverage," *IEEE Trans. Antennas Propag.*, vol. 62, no. 10, pp. 5365–5369, Oct. 2014.

[22] C. Morlaas, B. Souny, and A. Chabory, "Helical-ring antenna for hemispherical radiation in circular polarization," *IEEE Trans. Antennas Propag.*, vol. 63, no. 11, pp. 4693–4701, Nov. 2015.

[23] Y.-X. Sun, K. W. Leung, and J. Ren, "Dual-band circularly polarized antenna with wide axial ratio beamwidths for upper hemispherical coverage," *IEEE Access*, vol. 6, pp. 58132–58138, 2018. [Online]. Available: https://ieeexplore.ieee.org/document/8488485/

[24] Z. Su, K. Klionovski, H. Liao, Y. Chen, A. Z. Elsherbeni, and A. Shamim, "Antenna-on-package design: Achieving near-isotropic radiation pattern and wide CP coverage simultaneously," *IEEE Trans. Antennas Propag.*, vol. 69, no. 7, pp. 3740–3749, Jul. 2021.

[25] H. W. Alsawaha and A. Safaai-Jazi, "Ultrawideband hemispherical helical antennas," *IEEE Trans. Antennas Propag.*, vol. 58, no. 10, pp. 3175–3181, Oct. 2010.

[26] Z. Zhang, Y. Cai, D. Wu, and Y.-X. Sun, "A wideband high-isolation omnidirectional antenna for in-band full duplex application," in *Proc. IEEE Conf. Antenna Meas. Appl. (CAMA)*, Dec. 2022, pp. 1–3.

[27] Y. Yu, Z. Shen, and S. He, "Compact omnidirectional antenna of circular polarization," *IEEE Antennas Wireless Propag. Lett.*, vol. 11, pp. 1466–1469, 2012.

[28] X.-W. Dai, Z.-Y. Wang, C.-H. Liang, X. Chen, and L.-T. Wang, "Multiband and dual-polarized omnidirectional antenna for 2G/3G/LTE application," *IEEE Antennas Wireless Propag. Lett.*, vol. 12, pp. 1492–1495, 2013.

[29] X. Yang, Y. Liu, and S.-X. Gong, "Design of a wideband omnidirectional antenna with characteristic mode analysis," *IEEE Antennas Wireless Propag. Lett.*, vol. 17, no. 6, pp. 993–997, Jun. 2018.

[30] D. Guo, K. He, Y. Zhang, and M. Song, "A multiband dual-polarized omnidirectional antenna for indoor wireless communication systems," *IEEE Antennas Wireless Propag. Lett.*, vol. 16, pp. 290–293, 2017.

[31] K. Fan, Z.-C. Hao, Q. Yuan, J. Hu, G. Q. Luo, and W. Hong, "Wideband horizontally polarized omnidirectional antenna with a conical beam for millimeter-wave applications," *IEEE Trans. Antennas Propag.*, vol. 66, no. 9, pp. 4437–4448, Sep. 2018.

[32] S. Ranvier et al., "Low-cost planar omnidirectional antenna for mm-Wave applications," *IEEE Antennas Wireless Propag. Lett.*, vol. 7, pp. 521–523, 2008.

[33] H. Liu, J. Liu, and J. Song, "Miniature and near-3D omnidirectional antenna based on simple structure for UHF band RFID tag," in *Proc. Int. Appl. Comput. Electromagn. Soc. Symp. (ACES-China)*, Dec. 2022, pp. 1–2.

[34] Z. Liu, S. Lin, P. Li, Y. Wang, and X. Zhang, "Design and analysis of an omnidirectional printed inverted-f antenna with quasi-isotropic radiation," in *Proc. IEEE Microw., Antennas, Propagat. Conf. (MAPCON)*, Dec. 2022, pp. 2059–2062.

[35] S. Lin, X.-B. Wei, X. Zhang, H.-J. Zhang, and X. Zhang, "Simulation analysis of a broadband high-gain omnidirectional printed antenna for mobile communications," in *Proc. IEEE Int. Symp. Antennas Propagat. USNC-URSI Radio Sci. Meeting (AP-S/URSI)*, Jul. 2022, pp. 727–728.
[36] C.-X. Mao, M. Khalily, P. Xiao, T. W. C. Brown, and S. Gao, "Planar sub-millimeter-wave array antenna with enhanced gain and reduced sidelobes for 5G broadcast applications," *IEEE Trans. Antennas Propag.*, vol. 67, no. 1, pp. 160–168, Jan. 2019.
[37] K. Paramayudha, S. J. Chen, W. Withayachumnankul, and C. Fumeaux, "Frequency-reconfigurable circularly polarized omnidirectional antenna," *IEEE Trans. Antennas Propag.*, vol. 70, no. 8, pp. 7205–7210, Aug. 2022.
[38] R. Chopra, A. Agarwal, and R. Lakhmani, "A broadband planar Bow-Tie antenna with quasi-isotropic coverage," in *Proc. IEEE Indian Conf. Antennas Propag. (InCAP)*, Dec. 2021, pp. 420–422.
[39] S. M. Radha, G. Shin, P. Park, and I.-J. Yoon, "Realization of electrically small, low-profile quasi-isotropic antenna using 3D printing technology," *IEEE Access*, vol. 8, pp. 27067–27073, 2020.
[40] J.-M. Floch, B. El Jaafari, and A. El Sayed Ahmed, "New compact broadband GSM/UMTS/LTE antenna realised by 3D printing," in *Proc. 9th Eur. Conf. Antennas Propagat. (EuCAP)*, Apr. 2015, pp. 1–4.
[41] Z. Su, K. Klionovski, R. M. Bilal, and A. Shamim, "3D printed near-isotropic asymmetric dipole antenna-on-package for IoT applications," in *Proc. IEEE Indian Conf. Antennas Propogation (InCAP)*, Dec. 2018, pp. 1–3.
[42] Z. Su, K. Klionovski, R. M. Bilal, and A. Shamim, "3D printed antenna-on-package with near-isotropic radiation pattern for IoT (WiFi based) applications," in *Proc. IEEE Int. Symp. Antennas Propagat. USNC/URSI Nat. Radio Sci. Meeting*, Jul. 2018, pp. 1431–1432.
[43] H. Liao, Q. Zhang, M. A. Karimi, Y.-H. Kuo, N. Mishra, and A. Shamim, "An additively manufactured 3-D antenna-in-package with quasi-isotropic radiation for marine animals monitoring system," *IEEE Antennas Wireless Propag. Lett.*, vol. 18, no. 11, pp. 2384–2388, Nov. 2019.
[44] Y. Yuan, S. J. Chen, and C. Fumeaux, "A 3D-printed hybrid dielectric resonator antenna with low cross-polarization," in *Proc. Int. Symp. Antennas Propagat. (ISAP)*, Oct. 2022, pp. 79–80.
[45] O. H. Kwon, W. B. Park, S. Lee, J. M. Lee, Y. M. Park, and K. C. Hwang, "Super-wideband Spidron fractal cube antenna using 3D printing technology," in *Proc. Int. Symp. Antennas Propagat. (ISAP)*, Oct. 2018, pp. 1–2.
[46] Y. Zhang, Y. Zhang, D. Li, Z. Niu, and Y. Fan, "Compact vertically polarized omnidirectional ultra-wideband antenna and its band-notched filtering application," *IEEE Access*, vol. 7, pp. 101681–101688, 2019.
[47] P. Ratajczak, "Design of a 3D printed omnidirectional antenna for 60 GHz application," in *Proc. 13th Eur. Conf. Antennas Propag. (EuCAP)*, Mar. 2019, pp. 1–4.
[48] J. Huang, Q. Qin, and J. Wang, "A review of stereolithography: Processes and systems," *Processes*, vol. 8, no. 9, p. 1138, Sep. 2020. [Online]. Available: https://www.mdpi.com/2227-9717/8/9/1138
[49] M. Pagac et al., "A review of vat photopolymerization technology: Materials, applications, challenges, and future trends of 3D printing," *Polymers*, vol. 13, no. 4, p. 598, Feb. 2021. [Online]. Available: https://www.mdpi.com/2073-4360/13/4/598
[50] K. Lomakin, M. Sippel, K. Helmreich, and G. Gold, "Design and analysis of 3D printed slotted waveguides for D-band using stereolithography and electroless silver plating," in *Proc. IEEE/MTT-S Int. Microw. Symp. (IMS)*, Aug. 2020, pp. 177–180. [Online]. Available: https://ieeexplore.ieee.org/document/9223819/
[51] K. Lomakin, G. Gold, and K. Helmreich, "Analytical waveguide model precisely predicting loss and delay including surface roughness," *IEEE Trans. Microw. Theory Techn.*, vol. 66, no. 6, pp. 2649–2662, Jun. 2018. [Online]. Available: https://ieeexplore.ieee.org/document/8356729/
[52] G. Gold and K. Helmreich, "A physical model for skin effect in rough surfaces," in *Proc. 42nd Eur. Microw. Conf.*, Oct. 2012, pp. 1011–1014. [Online]. Available: http://ieeexplore.ieee.org/document/6459235/
[53] G. Gold and L. Engel, "Typical offset of usable antenna bandwidth due to surface roughness," in *Proc. IEEE 22nd Annu. Wireless Microw. Technol. Conf. (WAMICON)*, Apr. 2022, pp. 1–4. [Online]. Available: https://ieeexplore.ieee.org/document/9786180/
[54] L. Klein, K. Lomakin, M. Sippel, K. Helmreich, and G. Gold, "Additively manufactured six-port for mm-Wave applications," in *Proc. 50th Eur. Microw. Conf. (EuMC)*, Jan. 2021, pp. 384–387. [Online]. Available: https://ieeexplore.ieee.org/document/9338044/
[55] K. Lomakin et al., "SLA-printed 3-D waveguide paths for e-band using electroless silver plating," *IEEE Trans. Compon., Packag. Manuf. Technol.*, vol. 9, no. 12, pp. 2476–2481, Dec. 2019. [Online]. Available: https://ieeexplore.ieee.org/document/8758346/
[56] K. Lomakin, S. Alhasson, and G. Gold, "Additively manufactured amplitude tapered slotted waveguide array antenna with horn aperture for 77 GHz," *IEEE Access*, vol. 10, pp. 44271–44277, 2022.
[57] L. Engel, K. Lomakin, G. Gold, T. Pfahler, J. Schür, and M. Vossiek, "3D printed waveguide transition for 77 GHz radar applications," in *Proc. 14th German Microw. Conf. (GeMiC)*, May 2022, pp. 13–16.
[58] K. Lomakin, L. Engel, J. Fleischmann, and G. Gold, "Additively manufactured wavemode transition for broadband E-band applications," in *Proc. IEEE MTT-S Int. Microw. Symp. (IMS)*, Jun. 2021, pp. 138–141. [Online]. Available: https://ieeexplore.ieee.org/document/9574889/
[59] B. Deutschmann and A. F. Jacob, "A full W-band waveguide-to-differential microstrip transition," in *Proc. IEEE MTT-S Int. Microw. Symp. (IMS)*, Jun. 2019, pp. 335–338.
[60] C. A. Balanis, *Antenna Theory: Analysis and Design*, 3rd ed. Hoboken, NJ, USA: Wiley, 2005.
[61] K. Lomakin et al., "3D printed slotted rectangular hollow waveguides," in *Proc. IEEE MTT-S Int. Microw. Symp. (IMS)*, Boston, MA, USA, Jun. 2019, pp. 342–345. [Online]. Available: https://ieeexplore.ieee.org/document/8700864/
[62] K. Lomakin, J. Schur, and G. Gold, "Design optimization of pyramidal horn antennas for 3D printing in the mm-Wave range," in *Proc. 16th Eur. Conf. Antennas Propagat. (EuCAP)*, Madrid, Spain, Mar. 2022, pp. 1–4. [Online]. Available: https://ieeexplore.ieee.org/document/9769314/

LUKAS ENGEL (Graduate Student Member, IEEE) was born in Ochsenfurt, Germany, in 1992. He received the B.Sc. and M.Sc. degrees in electrical engineering from Friedrich-Alexander-Universität Erlangen–Nürnberg (FAU), Erlangen, Germany, in 2017 and 2019, respectively, where he is currently pursuing the Ph.D. degree.

In 2019, he joined the Institute of Microwaves and Photonics (LHFT), FAU. His current research interests include antenna design, 3D-printed mm-Wave components, radar hardware, radar signal processing, and machine learning in radar applications.

DANTI KHOURI was born in Al-Malikiyah, Syria, in 1996. He received the B.Sc. degree in electrical engineering from Friedrich-Alexander-Universität Erlangen–Nürnberg, where he is currently pursuing the M.Sc. degree. In his master's thesis, he deals with a sensor fusion from an imaging radar and a depth camera.

KONSTANTIN LOMAKIN received the B.Sc. degree in electrical engineering and the M.Sc. degree in information and communication technology from Friedrich-Alexander-Universität Erlangen–Nürnberg in 2013 and 2015, respectively, where he is a member of the Microwave Assembly and Interconnects Group with the Institute of Microwaves and Photonics. His research interests include signal integrity, EM simulation and modeling, as well as 3D-printed mm-Wave components. He is also the Co-Founder and a CTO of Golden Devices GmbH.

ANDREAS HOFMANN (Graduate Student Member, IEEE) was born in Bayreuth, Germany, in 1990. He received the M.Sc. degree in electrical engineering from Friedrich-Alexander-Universität Erlangen–Nürnberg, Erlangen, Germany, in 2016, where he is currently pursuing the Ph.D. degree with the Institute of Microwave and Photonics (LHFT). His current research interests include radar systems, waveguide components, and additive manufacturing. He is the Co-Founder of Golden Devices GmbH.

MICHA KLEINLEIN received the B.Sc. degree in electrical engineering from Friedrich-Alexander-Universität Erlangen–Nürnberg in 2021, where he is currently pursuing the master's degree with the Microwave Assembly and Interconnects Group, Institute of Microwaves and Photonics. His research interests include signal integrity, EM-modeling, and 3D-printed mm-Wave components.

INGRID ULLMANN (Member, IEEE) received the M.Sc. degree in electrical engineering and the Ph.D. degree from Friedrich-Alexander-Universität Erlangen–Nürnberg, Erlangen, Germany, in 2016 and 2021, respectively, where she is currently a Postdoctoral Fellow and the Head of the Research Group "Wave-Based Imaging Systems," Institute of Microwaves and Photonics. In 2022, she spent one month as a Visiting Researcher with the Microwave Sensing, Signals and Systems Group, Delft University of Technology, Delft, The Netherlands. Her research interests include radar imaging and radar signal processing for nondestructive testing, security screening, medical radar, and automotive applications. She received the Argus Science Award (sponsored by Airbus Defense and Space, currently Hensoldt) in 2016 and the EuRAD Conference Prize in 2019. She serves as a Reviewer for the European Radar Conference and various journals in the field of microwaves. Since 2022, she has been an Associate Editor for the IEEE TRANSACTIONS ON RADAR SYSTEMS. She is a member of the IEEE CRFID Technical Committee on Motion Capture and Localization.

MARTIN VOSSIEK (Fellow, IEEE) received the Ph.D. degree from Ruhr-Universität Bochum, Bochum, Germany, in 1996. In 1996, he joined Siemens Corporate Technology, Munich, Germany, where he was the Head of the Microwave Systems Group from 2000 to 2003. Since 2003, he has been a Full Professor with Clausthal University, Clausthal-Zellerfeld, Germany. Since 2011, he has been the Chair of the Institute of Microwaves and Photonics (LHFT), Friedrich-Alexander-Universität Erlangen–Nürnberg, Erlangen, Germany. He has authored or coauthored more than 350 articles. His research has led to more than 100 granted patents. His current research interests include radar, microwave systems, wave-based imaging, transponders, RF identification, communication, and wireless sensor and locating systems. He has received numerous best paper prizes and other awards. In 2019, he was awarded the Microwave Application Award by the IEEE MTT Society for Pioneering Research in Wireless Local Positioning Systems. From 2013 to 2019, he served as an Associate Editor for the IEEE TRANSACTIONS ON MICROWAVE THEORY AND TECHNIQUES. Since October 2022, he has been serving as an Associate Editor-in-Chief for IEEE TRANSACTIONS ON RADAR SYSTEM. He has been a member of a organizing committees and a technical program committees for many international conferences and has served on the review boards of numerous technical journals. He is a member of the German National Academy of Science and Engineering (acatech) and of the German Research Foundation (DFG) Review Board. He is a member of the IEEE Microwave Theory and Technology Technical Committees for MTT-24 Microwave/mm-Wave Radar, Sensing, and Array Systems; MTT-27 Connected and Autonomous Systems (as the Founding Chair); and MTT-29 Microwave Aerospace Systems. He also serves on the advisory board of the IEEE CRFID Technical Committee on Motion Capture and Localization.

GERALD GOLD (Member, IEEE) received the Diploma degree in mechatronics and the Dr. Eng. degree from Friedrich-Alexander University Erlangen-Nürnberg, Erlangen, Germany, in 2009 and 2016, respectively, where he has been with the Institute of Microwaves and Photonics as a Research Assistant since 2010. He became the Group Leader of the Microwave Assembly and Interconnects Group in 2018. His research interests include 3D-printed microwave components, electromagnetic interaction with non-ideal surfaces, and automation of RF-measurements. He is a member of the IEEE MTT-S Technical Committee MTT-16, and the Co-Founder and the Research and Development Supervisor of Golden Devices.